

Development of a highly stable nickel-foam-based boron monosulfide–graphene electrocatalyst with a high current density for the oxygen evolution reaction

Linghui Li, Norinobu Watanabe, Cheng Jiang, Akiyasu Yamamoto, Takeshi Fujita, Masashi Miyakawa, Takashi Taniguchi, Hideo Hosono & Takahiro Kondo

To cite this article: Linghui Li, Norinobu Watanabe, Cheng Jiang, Akiyasu Yamamoto, Takeshi Fujita, Masashi Miyakawa, Takashi Taniguchi, Hideo Hosono & Takahiro Kondo (2023) Development of a highly stable nickel-foam-based boron monosulfide–graphene electrocatalyst with a high current density for the oxygen evolution reaction, *Science and Technology of Advanced Materials*, 24:1, 2277681, DOI: [10.1080/14686996.2023.2277681](https://doi.org/10.1080/14686996.2023.2277681)

To link to this article: <https://doi.org/10.1080/14686996.2023.2277681>



© 2023 The Author(s). Published by National Institute for Materials Science in partnership with Taylor & Francis Group.



Published online: 20 Nov 2023.



Submit your article to this journal [↗](#)



Article views: 598







View related articles [↗](#)



View Crossmark data [↗](#)

Development of a highly stable nickel-foam-based boron monosulfide–graphene electrocatalyst with a high current density for the oxygen evolution reaction

Linghui Li^a, Norinobu Watanabe^a, Cheng Jiang^b, Akiyasu Yamamoto ^c, Takeshi Fujita ^d, Masashi Miyakawa ^e, Takashi Taniguchi ^e, Hideo Hosono ^{e,f} and Takahiro Kondo ^{g,h}

^aGraduate School of Pure and Applied Sciences, University of Tsukuba, Tsukuba, Japan;

^bCentre for Hydrogenenergy, College of Materials Science and Technology, Nanjing University of Aeronautics and Astronautics, Nanjing, P. R. China;

^cInstitute of Engineering, Tokyo University of Agriculture and Technology, Tokyo, Japan;

^dSchool of Engineering Science, Kochi University of Technology, Kochi, Japan;

^eResearch Center for Materials Nanoarchitectonics, National Institute for Materials Science, Tsukuba, Japan;

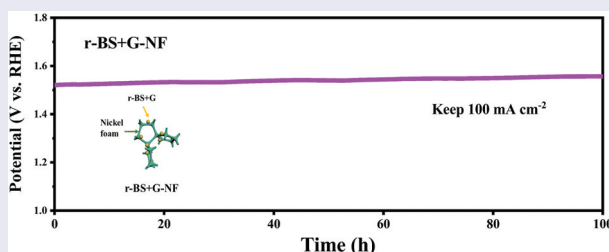
^fMDX Research Center for Element Strategy, Tokyo Institute of Technology, Yokohama, Japan;

^gDepartment of Materials Science, Tsukuba Research Center for Energy Materials Science, Institute of Pure and Applied Sciences, and R&D Center for Zero CO₂ Emission with Functional Materials, University of Tsukuba, Tsukuba, Japan;

^hAdvanced Institute for Materials Research, Tohoku University, Sendai, Japan

ABSTRACT

As an important part of water splitting, the oxygen evolution reaction (OER) requires efficient, low-cost, and stable catalysts to overcome its sluggish kinetic barrier. In this study, based on previously reported OER catalyst materials of boron monosulfide mixed with graphene (r-BS+G), nickel foam (NF) is introduced as a supporting material for an r-BS+G electrocatalyst. The resulting r-BS+G-NF exhibits a very low overpotential at 10 (245 mV), 100 (308 mV), and 500 (405 mV) mA cm⁻², with a low Tafel slope (56 mV dec⁻¹). In addition, r-BS+G-NF exhibits high durability and can maintain high activity for more than 100 h at 100 mA cm⁻². This is in sharp contrast to the catalyst without graphene (r-BS+NF), which shows lower durability. The results suggest that the unique morphology of the NF provides a large electrochemically active area and exposes more active sites on the surface of the prepared electrocatalyst, while the flexible graphene sheets play an important role as a support for effectively combining r-BS and NF. Consequently, the self-supporting structure can improve the OER performance as well as stability. Therefore, this study provides a promising strategy for use as an efficient and stable OER catalyst at high current densities.



IMPACT STATEMENT

In the realm of electrocatalysis and the quest for sustainable energy conversion and storage technologies, our research introduces a distinctive contribution in the form of a nickel-foam-based boron monosulfide – graphene electrocatalyst (r-BS+G-NF) for the Oxygen Evolution Reaction (OER). Thanks to the porous structure of nickel foam and the important role of graphene in combining r-BS and nickel foam, r-BS+G-NF exhibits high catalytic activity and long durability for up to 100 hours. The findings presented in this paper represent a significant advancement in the field of electrocatalysis, with the potential to impact the development of cleaner and more efficient energy conversion and storage technologies.

1. Introduction

The excessive consumption and subsequent shortage of fossil fuels have led to environmental pollution and

energy crises. Thus, the development of renewable, clean, efficient, and environmentally friendly energy sources has become increasingly important to combat these issues. Hydrogen, which has the advantages of

CONTACT Takahiro Kondo  takahiro@ims.tsukuba.ac.jp  Department of Materials Science, Tsukuba Research Center for Energy Materials Science, Institute of Pure and Applied Sciences, and R&D Center for Zero CO₂ Emission with Functional Materials, University of Tsukuba, Tsukuba 305-8573, Japan
 Supplemental data for this article can be accessed online at <https://doi.org/10.1080/14686996.2023.2277681>.

© 2023 The Author(s). Published by National Institute for Materials Science in partnership with Taylor & Francis Group.

This is an Open Access article distributed under the terms of the Creative Commons Attribution License (<http://creativecommons.org/licenses/by/4.0/>), which permits unrestricted use, distribution, and reproduction in any medium, provided the original work is properly cited. The terms on which this article has been published allow the posting of the Accepted Manuscript in a repository by the author(s) or with their consent.

a high energy density and zero carbon emissions, is considered one of the most promising energy sources [1]. Currently, the preparation of hydrogen primarily involves natural gas reforming, petroleum cracking, coal gasification, and electrochemical water splitting [2]. Water splitting plays an important role in hydrogen production because of its environmental friendliness and high purity [3,4].

Electrochemical water splitting involves two half-reactions, namely the hydrogen and oxygen evolution reactions (HER and OER, respectively) [5]. The HER involves a dynamic two-electron-transfer process. However, the OER is less efficient than the HER, involving an uphill complex four-electron transfer reaction, which is the main energy barrier limiting the efficiency of water decomposition and conversion [6]. Therefore, the introduction of an efficient OER catalyst can significantly reduce the overpotential and improve catalytic efficiency. Noble metal oxides, such as RuO_2 and IrO_2 , are recognised as active catalysts for the OER [7]. However, the scarcity and high price of precious metals have significantly hindered their widespread practical application. Therefore, the development of efficient and stable non-noble metal-based catalysts for the OER is a current research priority.

Currently, most electrocatalysts reported for the OER are based on transition-metal materials. In the past few years, transition non-noble metals, such as Ni, Co, Cu, Fe, and Mo, and compounds containing sulfides, selenides, tellurides, carbides, and nitrides have shown high catalytic performances [8–14], some of which even exceed those of the corresponding oxides and hydroxides. The exposure rate of metal-free catalysts is considerably lower than that of metal-based catalysts because the synthesis and performance of many metal-free catalysts require further improvement [15].

In addition, hydrogen and oxygen bubbles are easily generated during the water-splitting process, especially under a high current density, which separates some active materials from the substrate, thus greatly reducing the activity [16]. Further, the self-supporting structure is the most effective way to avoid using the adhesive that will bury some of the active part. Three-dimensional (3D) substrates, such as metal foams and meshes, are better suited for industrial applications because of their unique characteristics. The 3D framework of these substrates offers advantages such as high catalyst loading, smooth mass transfer, and improved electrode contact within the 3D networks. Metal foams with interconnected pore structures can be obtained through the high-temperature sintering of metals. This structure provided a larger surface area and enhanced material transport pathways, resulting in increased catalyst loading and superior mass transfer capabilities [9].

Among 3D substrates, 3D nickel foam (NF) with a high conductivity, large surface area, good stability, and affordability, is considered a promising substrate [17–19].

Previously, we reported a rhombohedral boron monosulfide (r-BS) mixed with graphene (r-BS+G) as a new metal-free electrocatalyst, which showed promising electrocatalytic activity with much better performance than that of most reported metal-free catalysts in 1 M KOH solution [20]. The catalytic performance of the r-BS+G electrocatalyst was maintained for 500 cyclic voltammetry (CV) cycles and declined after 1000 CV cycles due to the separation of materials from the electrode [20]. In this work, to solve this problem and increase the stability for r-BS+G catalyst, we used NF as a self-supporting working electrode (r-BS+G-NF). After dropping the sample ink onto the NF, the stability of the r-BS+G significantly improved. Specifically, r-BS+G-NF could remain stable for over 100 h at 100 mA cm^{-2} , and the Tafel slope was significantly reduced from 210 mV dec^{-1} (r-BS+G) to 56 mV dec^{-1} , which provided more possibilities for future practical applications. In addition, r-BS+G-NF exhibited superior performance and stability as an electrocatalyst for the OER compared with the case of without graphene (r-BS+NF), which suggests that flexible graphene sheets played an important role as a support for effectively combining r-BS and NF.

2. Method

2.1 Materials

Amorphous boron (>99.5%) was prepared by the decomposition of B_2H_6 (Primary Metal Chemical, Kanagawa, Japan). Sulfur (99%) was purchased from Wako Pure Chemical Industries Ltd. (Osaka, Japan). Graphene nanoplates (GNPs) (5–7 layers), Nafion (5 wt % in lower aliphatic alcohols and water), KOH (97%), and commercial RuO_2 (99.9%) were purchased from Sigma-Aldrich (Japan). NF (200 mm × 300 mm × 1.5 mm) was purchased from Amazon (Santuo). Solvents were purchased from commercial sources.

2.2 Synthesis of r-BS

r-BS was synthesised using a previously reported method [20–23]. Boron and sulfur were mixed in a 1:1 atomic ratio in a mortar and compressed at 200 kgf cm^{-2} to form pellets. The pellets were packed in hexagonal boron nitride (h-BN) capsules and sandwiched between NaCl and graphite discs to prepare the cells. The cells were heated at 1873 K for 40 min at 5.5 GPa using a belt-type high-pressure apparatus with a cylindrical bore diameter of approximately 32 mm [24], quenched, removed, and crushed into powder with a mortar and pestle.

2.3 Preparation of r-BS+G

To prepare r-BS+G, 5 mg of r-BS powder and 10 mg of GNPs were suspended in 1 mL of ethanol, followed by 1 h of bath sonication (500 W, 60 Hz, AS ONE Ltd., Japan). To generate an ink for electrochemical measurements, a Nafion solution (50 μL) was added to the r-BS+G mixture in ethanol.

2.4 Preparation of r-BS+G-NF, r-BS-NF, graphene-NF, and RuO₂-NF

The NF was pre-treated before being used in further experiments. It was further sonicated in acetone to remove surface oil stains, soaked in 20% hydrochloric acid (5 min) to remove surface oxide films, and cleaned via ultrasonication using distilled water and ethanol in sequence. Then, the prepared r-BS+G ink was dropped five times on the treated NF (10 μL every time, a total of 50 μL), and after drying, r-BS+G-NF was obtained. r-BS-, graphene-, and RuO₂-NFs were prepared similarly. The r-BS, graphene, and RuO₂ inks all contained 5 mg of active materials, 1 mL of ethanol, and 50 μL of Nafion.

2.5 Characterisation

Powder X-ray diffraction (XRD) analysis was carried out with a Cu K α X-ray source (wavelength $\lambda = 1.540598 \text{ \AA}$) using a Rigaku MiniFlex (Tokyo, Japan). XRD patterns were recorded using a D/teX Ultra silicon strip detector (Rigaku) at a speed of 0.05°s^{-1} up to $2\theta = 80^\circ$, where θ is the angle of incidence. Scanning electron microscopy (SEM) and electron probe microanalysis (EPMA) were conducted with an operating voltage of 10 kV using a JXA-8530F instrument (JEOL Ltd., Japan). Raman spectroscopy was performed using a multichannel Raman imaging system (ST Japan Inc., Tokyo, Japan) at an incident wavelength of 532 nm. X-ray photoelectron spectroscopy (XPS) measurements were carried out with a Mg K α X-ray source ($\lambda = 1253.6 \text{ eV}$) using a JPS 9010 TR spectrometer (JEOL Ltd.). The specimens were positioned on a strip of graphite tape. As electric charge accumulated in the specimen, it displaced the binding energy towards higher values. The extent of this charge build-up was standardised using the C 1s peaks of graphene and graphite tape at 284.6 eV.

2.6 Electrochemical measurements

All electrochemical measurements were performed using a CorrTest CS2350H electrochemical workstation in 1 M aqueous KOH with an H-type electrolytic cell (GOOSS UNION Co., Ltd., China; Figure S1). The prepared r-BS+G-NF acted as a self-supporting working electrode, Hg/HgO (1 M KOH,

aqueous) or Ag/AgCl was used as the reference electrode, and a Pt wire was used as the counter electrode. All the electrodes were purchased from BAS Inc., Japan, except for the active material and NF. Electrochemical data were calculated using a measured geometric area of 0.5 cm^2 to match the actual soaking area of KOH. This measured area was maintained for all testing processes. For each measurement, the prepared ink (50 μL) was dropped thrice onto the pre-treated NF to achieve a final catalyst loading of 0.5 mg cm^{-2} . Linear sweep voltammetry (LSV) curves were recorded at a scan rate of 5 mV s^{-1} , and the obtained potential was subjected to iR correction. The LSV curves recorded before and after 2000 CV cycles (1.20–1.55 V vs. reversible hydrogen electrode (RHE), scan rate = 100 mV s^{-1}) and the chronopotentiometry curves measured at 100 mA cm^{-2} for 20 or 100 h were compared to evaluate the electrocatalytic stability of the catalysts. The double-layer capacitance (C_{dl}) was used to examine the electrochemically active surface area (ECSA) in the potential range of 0.82–0.92 V vs. RHE. Electrochemical impedance spectroscopy (EIS) measurements were performed in the frequency range of 1×10^5 to 0.1 Hz at 1.6 V vs. RHE with a perturbation amplitude of 5 mV.

All experiments were conducted at ambient temperature ($298 \pm 2 \text{ K}$), and the electrode potential was converted to the RHE scale as follows:

$$E(\text{RHE}) = E(\text{Hg}/\text{HgO}) + 0.0591 \cdot \text{pH} + 0.108 \text{ V} = E(\text{Hg}/\text{HgO}) + 0.935 \text{ V (pH 14) and}$$

$$E(\text{RHE}) = E(\text{Ag}/\text{AgCl}) + 0.0591 \cdot \text{pH} + 0.199 \text{ V} = E(\text{Ag}/\text{AgCl}) + 1.026 \text{ V (pH 14)}$$

Thus, the reversible potential of water oxidation, namely 1.23 V vs. RHE at pH 14, could be calculated as 0.295 V vs. Hg/HgO/1.0 M KOH at pH 14 ($1.230 - 0.935 \text{ V} = 0.295 \text{ V}$) and 0.204 V vs. Ag/AgCl at pH 14 ($1.230 - 1.026 \text{ V} = 0.204 \text{ V}$).

2.7 iR correction

Ohmic loss correction was conducted for polarisation curves recorded on different support surfaces as $E_{\text{corrected}} = E - iR_u$, where $E_{\text{corrected}}$ is the iR -corrected potential, E is the measured potential, i is the measured current, and R_u is the series resistance measured by EIS.

3. Results and discussion

The XRD pattern of r-BS+G was a combination of those of r-BS and GNPs (Figure S2(a)). The XPS results confirmed that physically mixing r-BS and GNPs there did not shift the B 1s or S 2p peaks (Figure S3). When the r-BS+G sample ink was dropped onto a normal glassy carbon electrode (GCE) as the working electrode, it showed

a notable OER performance in 1 M KOH, and the overpotential of r-BS+G at 10 mA cm⁻² was 250 mV, which was 50 mV lower than that of commercial RuO₂ (Figure S4), as previously reported [20]. (The crystal and particle sizes of each sample are presented in Table S1 and Figure S5). However, the stability of r-BS+G was not as good; it could only maintain high performance for 500 CV cycles, which was ascribed to material separation from the GCE surface when oxygen bubbles were generated at a high current density, as reported previously [20]. In this study, NF was introduced as a support to improve the stability of an r-BS+G electrocatalyst (Figure 1). As shown in Figure 2(a), the NF has a porous structure, and the crisscross holes are conducive to gas precipitation and largely protect the catalyst against material loss caused by the generation of bubbles. After the sample ink was dropped onto the pretreated NF, the framework of NF supported the r-BS and GNP particles well, as shown in Figure 2(b). The light grey network is the nickel skeleton, the grey particles in the middle are r-BS, and the black particles are GNPs, as verified using EPMA (Figure 2(c)).

All electrochemical tests were performed in a 1.0 M KOH electrolyte using a standard three-electrode system. The prepared sample-NF was used as the working electrode. LSV was performed to obtain polarisation curves corrected by *iR*-compensation. As shown in Figure 3(a), bare NF exhibited a poor OER performance. The r-BS+G-NF electrocatalyst showed the best catalytic activity for the OER, and its overpotential at 10 mA cm⁻² was 245 mV, which was lower than those of r-BS-NF (272 mV), commercial RuO₂-NF (270 mV), graphene-NF (320 mV), and bare NF (351 mV). Remarkably, r-BS+G-NF presented high current densities of 100 and 500 mA cm⁻² at 308 and 430 mV for the OER, respectively, whereas for commercial RuO₂-NF, overpotentials of 365 and 513 mV were required to reach the same current densities (Figure S6).

The Tafel slope is another important factor for evaluating electrocatalysts (Figure 3(b)). The Tafel slope was obtained by the linear fitting of the corresponding LSV curves using the Tafel equation. The r-BS+G-NF electrocatalyst displayed the lowest Tafel slope of 56 mV dec⁻¹, while the Tafel slopes of r-BS-NF, RuO₂-NF, graphene-NF, and bare NF were 65,

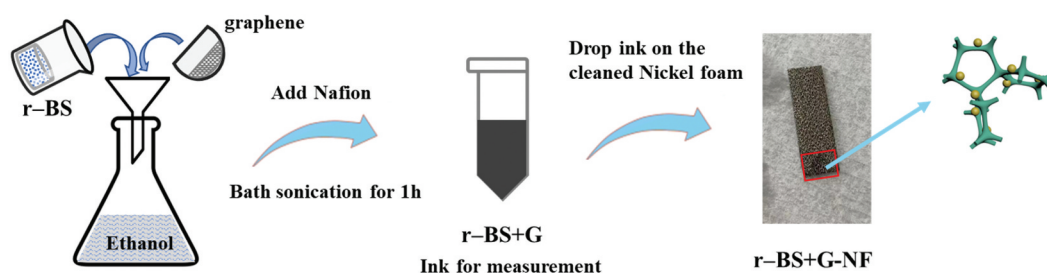


Figure 1. Schematic illustration of the synthesis of a nickel-foam-based boron monosulfide – graphene electrocatalyst (r-BS+G-NF).

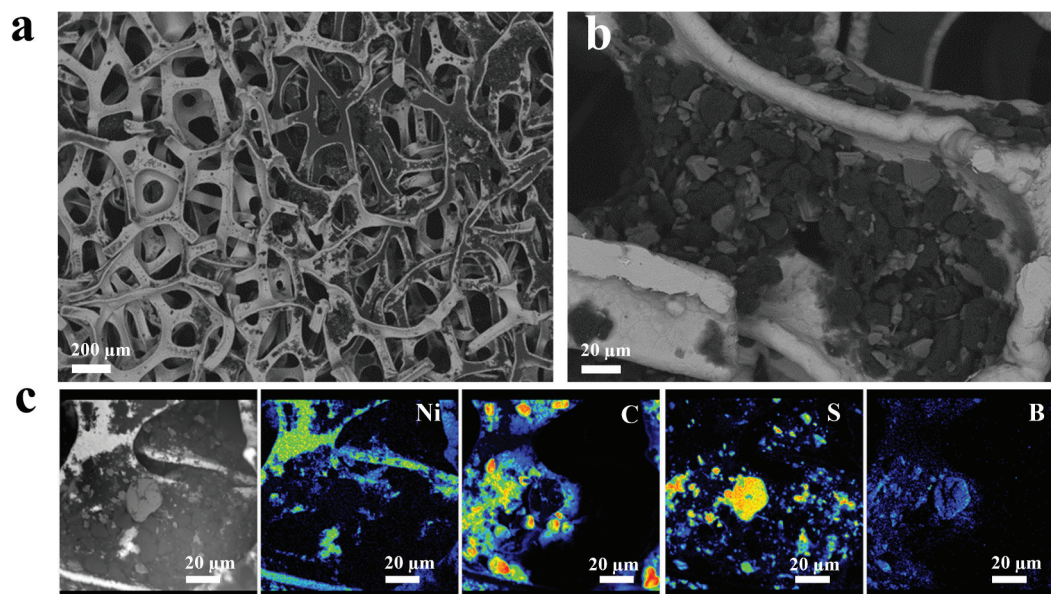


Figure 2. (a,b) Scanning electron microscopy (SEM) and (c) Electron probe microanalyzer (EPMA) images of the r-BS+G-NF electrocatalyst.

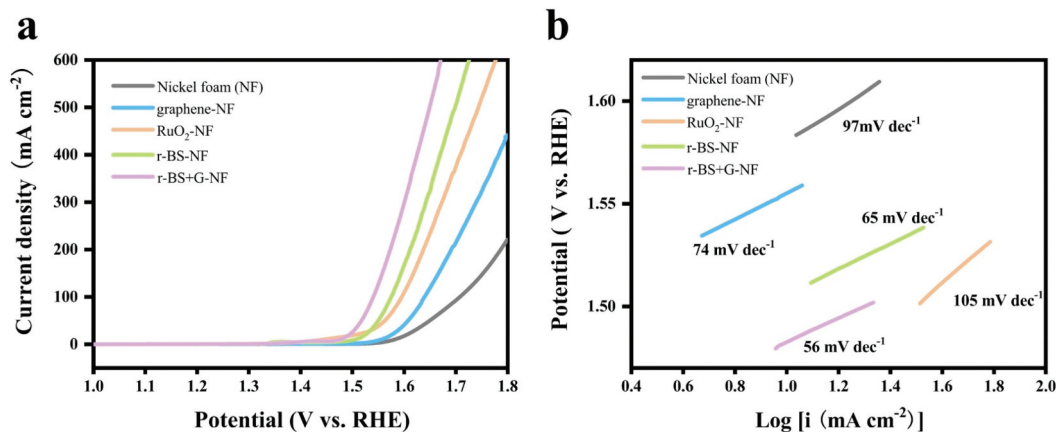


Figure 3. Electrochemical measurements of the as-prepared samples for the oxygen evolution reaction (OER): (a) Linear sweep voltammetry (LSV) curves and (b) Tafel slopes.

105, 74, and 97 mV dec^{-1} , respectively. The smaller Tafel slope of r-BS+G-NF indicates superior OER kinetics. In this regard, the performance of r-BS+G-NF was significantly better than that of the previous samples without the NF support, namely r-BS+G (210 mV dec^{-1}) [20]. This indicates that their rate-determining steps differ and/or that different reactions occur. A comparison of the OER performances of all samples is listed in Table S2. The value of r-BS+G-NF was better than those of recently reported NF-based catalysts (Table S3), showing its remarkable potential. In addition, CV was conducted on all of the catalysts over a wide electrochemical window, as shown in Figure S7, and a notable peak appears at $\sim 1.42 \text{ V vs. RHE}$ in all cases, which is ascribed to the reversible transformation of $\beta\text{-Ni}(\text{OH})_2$ into $\beta\text{-NiOOH}$ [25,26]. For r-BS+G-NF, r-BS-NF, and $\text{RuO}_2\text{-NF}$, this oxidation/reduction peak is much more intense than that for bare NF and graphene-NF, implying a larger amount of oxidation/reduction sites on the NF in the three former catalysts [25]. This is probably because the species produced on r-BS, r-BS+G, or RuO_2 (such as intermediate species on the active sites for the OER) diffuse to the NF, thereby creating new oxidation/reduction sites, which initiate this peak. Further careful analysis is required to understand the origin of the difference in the peak intensities near 1.42 V vs. RHE .

EIS was performed using an equivalent circuit to further explore the kinetics of the catalysts during electrocatalysis. The Nyquist diagrams of the experimental and fitting data for all samples measured at 1.6 V vs. RHE . As shown in Figure S8, the Nyquist plot was fitted using the Randles equivalent circuit model. r-BS+G-NF exhibits a smaller semicircle, indicating superior conductivity and more rapid electronic transport. The charge-transfer resistance (R_{ct}) can be obtained from the semicircle diameter drawn by EIS, where a lower value indicates faster dynamics [27]. The R_{ct} values of bare NF, graphene-NF, $\text{RuO}_2\text{-NF}$, r-BS-NF, and r-BS+G-NF were 2.27, 1.83, 1.56, 1.22,

and 0.72Ω , respectively. As described above, r-BS+G-NF exhibited the smallest R_{ct} , which implies increased electrochemical activity and/or an increased number of active sites. (Detailed information on the R_{ct} and R_{u} values is provided in Table S4).

Taken together, these results indicate that although NF can play an important role as a superior support material, for example by providing higher electronic conductivity, it cannot fully encapsulate the r-BS particles and thus cannot effectively provide sufficient conductivity to each r-BS particle. In contrast, flexible graphene can closely combine with r-BS, enabling each r-BS particle to obtain a certain degree of conductive support. Consequently, combining the superior large-scale NF support with graphene as the local flexible support material delivers the best performance, as shown in Figure 3.

The stability of the r-BS+G-NF was tested using CV and chronopotentiometry. As shown in Figure 4(a), after 2000 CV cycles between 1.20 and 1.55 V vs. RHE , r-BS+G-NF only showed limited degradation, and its morphology also exhibited limited changes (Figure S9), demonstrating high catalytic stability and promise for industrial applications. Meanwhile, the stability was also evaluated by chronopotentiometry. As shown in Figure 4(b), both the $\text{RuO}_2\text{-NF}$ and r-BS-NF showed a trend of continuously increasing voltage during a prolonged chronopotentiometry test at a constant current density of 100 mA cm^{-2} . This is in sharp contrast to the case of r-BS+G+NF, where a negligible change was observed (Figure 4(b)). Furthermore, r-BS+G-NF exhibited high durability, even for 100 h (Figure 4(c)). These results further suggest that as a support material for effectively combining r-BS and NF, the flexible graphene sheets played a critical role in stabilizing the electrocatalyst.

The element content and structure of r-BS+G-NF before and after electrocatalysis were studied by SEM/EDX and Raman spectroscopy. After electrocatalysis, the morphology of GNP changed slightly, while r-BS

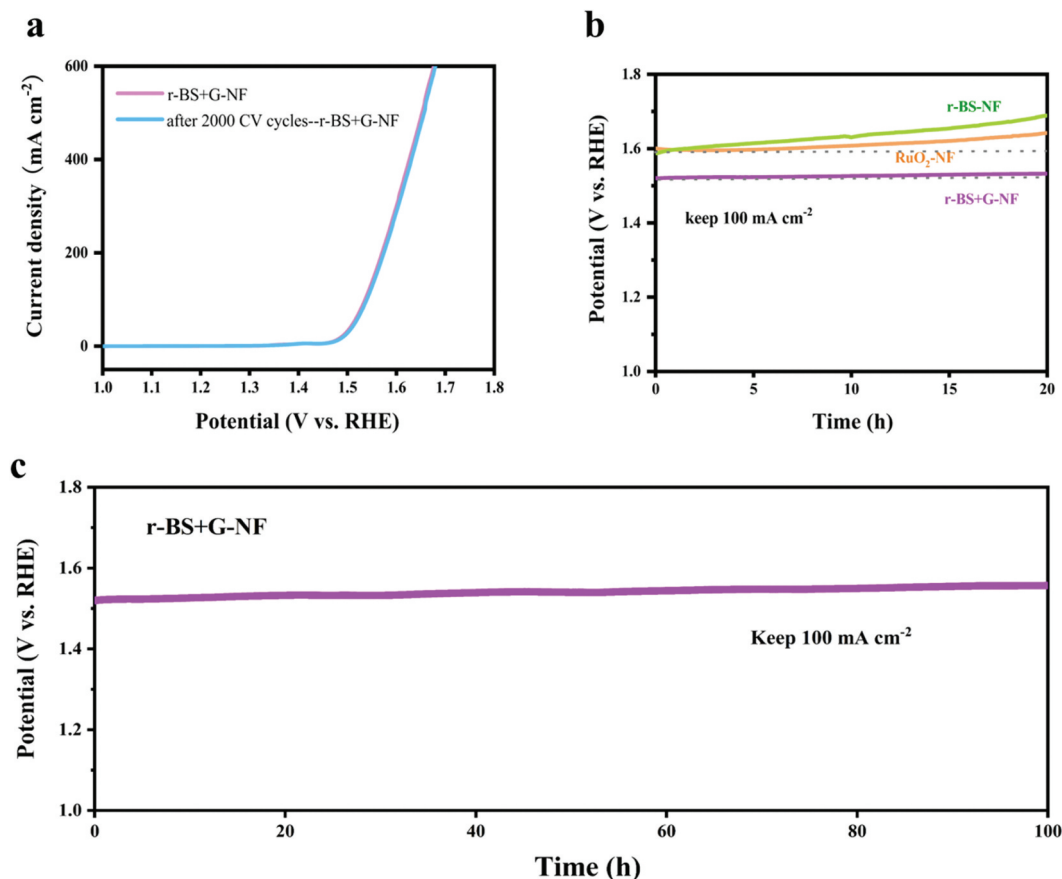


Figure 4. Evaluation of the stability of the as-prepared electrocatalyst. (a) LSV curves of the r-BS+G-NF electrocatalyst recorded before and after 2000 cyclic voltammetry cycles (1.2–1.55 V vs. RHE). (b,c) Chronopotentiometry curves of the as-prepared electrocatalysts at a constant current of 100 mA cm⁻² for (b) 20 h and (c) 100 h.

maintained its original appearance, and the EPMA mapping images showed that B, S, and C remained stable (Figure S9). Raman spectra of r-BS+G-NF recorded under various conditions are shown in Figure 5. There were three distinct peaks in the small-wavenumber region (Figure 5(a)) at 319, 687, and 1041 cm⁻¹, which can be attributed to the A1(3), E(4), and A1(4) modes of r-BS, respectively (Figure 5(b)) [28]. The large-wavenumber region (Figure 5(c)) did not demonstrate major spectral changes, such as a peak shift or (dis)appearance, in r-BS+G-NF during the electrochemical measurements. There were three major peaks in the large-wavenumber region at 1383, 1582, and 2705 cm⁻¹, which can be attributed to the D-, G-, and 2D-bands of graphene, respectively (Figure 5(d)) [29]. These results demonstrate the stability of the prepared r-BS+G-NFs and provide a strong basis for future applications.

In addition, the ECSA was evaluated based on the C_{dl} measurement results [30]. Specifically, CVs were tested from 0.8 to 0.9 V vs. RHE at a scan rate between 20 and 100 mV s⁻¹ (Figure S10). By obtaining the ECSA data under the same conditions, it can be observed that r-BS+G-NF showed a larger C_{dl} (29.4

mF cm⁻²) than r-BS-NF (21 mF cm⁻²), RuO₂-NF (27.8 mF cm⁻²), graphene-NF (25.7 mF cm⁻²), and bare NF (12.4 mF cm⁻²). A larger C_{dl} value suggests a larger electrochemical surface area for the electrocatalyst.

4. Conclusion

A freestanding high-efficiency electrocatalyst (r-BS+G-NF) was synthesised using a simple method. Benefiting from the newly reported active material (r-BS) and 3D structure, the electrocatalyst exhibited significant OER activity, where flexible graphene sheets were suggested to play an important role as a support for effectively combining r-BS and NF. It required small overpotentials at high current densities ($\eta_{10} = 245$ mV, $\eta_{100} = 308$ mV, and $\eta_{500} = 405$ mV) and exhibited a low Tafel slope (56 mV dec⁻¹). In addition, it showed good stability after maintaining the current density at 100 mA cm⁻² for 100 h. Therefore, this study improves the deficiency of pure metal-free catalysts and provides a method to produce a catalyst with a novel morphology, high activity, and stability under a high current density, thereby making the industrialisation of relevant energy devices possible.

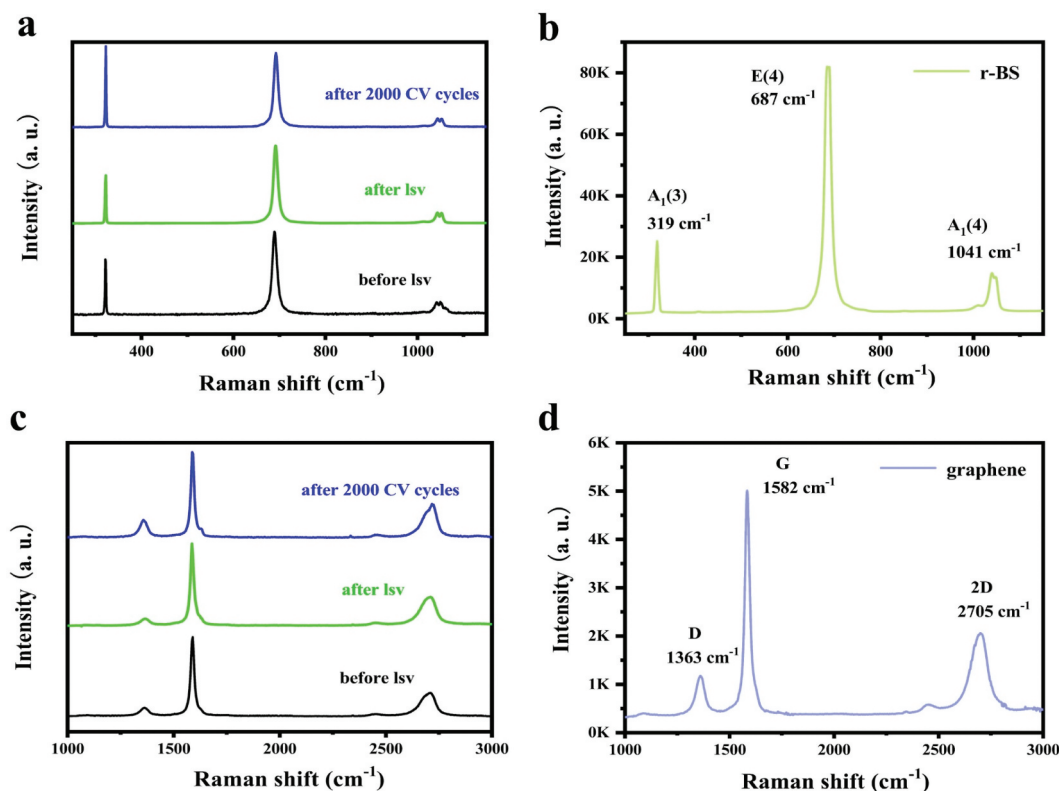


Figure 5. (a,c) Raman spectra of the r-BS+G-NF electrocatalyst under various conditions at (a) small wavenumbers (measured by focusing on r-BS particles) and (c) Large wavenumbers (measured by focusing on graphene particles). Raman spectra of the unmodified r-BS (b) and graphene (d) Powders.

Disclosure statement

No potential conflict of interest was reported by the author(s).


Funding

This work was supported by the Japan Science and Technology Agency (JST) through the Adaptable and Seamless Technology Transfer Program through Target-driven R&D (A-STEP) [grant number JPMJTR22T4]; the MEXT Element Strategy Initiative to Form Core Research Center [grant number JPMXP0112101001]; JSPS KAKENHI [grant numbers JP18K18989, JP19H02551, JP19H05790, JP19H05046:A01, JP21H05012, JP22K18964, and JP21H00015:B01 Hydrogenomics]; MHI Innovation Accelerator LLC; and TIAKakehashi collaborative research program (2022).

ORCID

Akiyasu Yamamoto  <http://orcid.org/0000-0001-6346-3422>

Takeshi Fujita  <http://orcid.org/0000-0002-2318-0433>

Masashi Miyakawa  <http://orcid.org/0000-0002-0838-8156>

Takashi Taniguchi  <http://orcid.org/0000-0002-1467-3105>

Hideo Hosono  <http://orcid.org/0000-0001-9260-6728>

Takahiro Kondo  <http://orcid.org/0000-0001-8457-9387>

References

- [1] Dincer I. Renewable energy and sustainable development: a crucial review. *Renew Sust Energ Rev.* 2000 Jun;4(2):157–175. doi: [10.1016/S1364-0321\(99\)00011-8](https://doi.org/10.1016/S1364-0321(99)00011-8)
- [2] Schlapbach L, Züttel A. Hydrogen-storage materials for mobile applications. *Nature.* 2001 Nov;414 (6861):353–358. doi: [10.1038/35104634](https://doi.org/10.1038/35104634)
- [3] Chen J, Chen C, Qin M, et al. Reversible hydrogen spillover in Ru-WO_{3-x} enhances hydrogen evolution activity in neutral pH water splitting. *Nat Commun.* 2022 Sep;13(1):5382. doi: [10.1038/s41467-022-33007-3](https://doi.org/10.1038/s41467-022-33007-3)
- [4] Zhou P, Navid IA, Ma Y, et al. Solar-to-hydrogen efficiency of more than 9% in photocatalytic water splitting. *Nature.* 2023 Jan;613(7942):66–70. doi: [10.1038/s41586-022-05399-1](https://doi.org/10.1038/s41586-022-05399-1)
- [5] Zhai P, Xia M, Wu Y, et al. Engineering single-atomic ruthenium catalytic sites on defective nickel-iron layered double hydroxide for overall water splitting. *Nat Commun.* 2021 Jul;12(1):4587. doi: [10.1038/s41467-021-24828-9](https://doi.org/10.1038/s41467-021-24828-9)
- [6] Jiang K, Luo M, Peng M, et al. Dynamic active-site generation of atomic iridium stabilized on nanoporous metal phosphides for water oxidation. *Nat Commun.* 2020 Jun;11:2701. doi: [10.1038/s41467-020-16558-1](https://doi.org/10.1038/s41467-020-16558-1)
- [7] Yan Z, Sun H, Chen X, et al. Anion insertion enhanced electrodeposition of robust metal hydroxide/oxide electrodes for oxygen evolution. *Nat Commun.* 2018 Jun;9(1):2373. doi: [10.1038/s41467-018-04788-3](https://doi.org/10.1038/s41467-018-04788-3)
- [8] Masa J, Schuhmann W. The role of non-metallic and metalloid elements on the electrocatalytic activity of cobalt and nickel catalysts for the oxygen evolution

- reaction. *ChemCatChem*. 2019 Aug;11(24):5842–5854. doi: [10.1002/cctc.201901151](https://doi.org/10.1002/cctc.201901151)
- [9] Li Z, Zhang X, Ou C, et al. Transition metal-based self-supported anode for electrocatalytic water splitting at a large current density. *Coord Chem Rev*. 2023 Nov;495:215381. doi: [10.1016/j.ccr.2023.215381](https://doi.org/10.1016/j.ccr.2023.215381)
- [10] Czioska S, Wang J, Teng X, et al. Hierarchically structured CuCo_2S_4 nanowire arrays as efficient bifunctional electrocatalyst for overall water splitting. *ACS Sustain Chem Eng*. 2018 Jul;6(9):11877–11883. doi: [10.1021/acssuschemeng.8b02155](https://doi.org/10.1021/acssuschemeng.8b02155)
- [11] Sivanantham A, Shanmugam S. Nickel selenide supported on nickel foam as an efficient and durable non-precious electrocatalyst for the alkaline water electrolysis. *Appl Catal B*. 2017 Apr;203:485–493. doi: [10.1016/j.apcatb.2016.10.050](https://doi.org/10.1016/j.apcatb.2016.10.050)
- [12] Majhi KC, Karfa P, Madhuri R. Bimetallic transition metal chalcogenide nanowire array: an effective catalyst for overall water splitting. *Electrochim Acta*. 2019 Sep;318:901–912. doi: [10.1016/j.electacta.2019.06.106](https://doi.org/10.1016/j.electacta.2019.06.106)
- [13] Guo M, Qayum A, Dong S, et al. In situ conversion of metal (Ni, Co or Fe) foams into metal sulfide (Ni_3S_2 , Co_9S_8 or FeS) foams with surface grown N-doped carbon nanotube arrays as efficient superaerophobic electrocatalysts for overall water splitting. *J Mater Chem A*. 2020 Apr;8(18):9239–9247. doi: [10.1039/D0TA02337J](https://doi.org/10.1039/D0TA02337J)
- [14] Luque-Centeno JM, Martínez-Huerta MV, Sebastián D, et al. Bifunctional N-doped graphene Ti and Co nanocomposites for the oxygen reduction and evolution reactions. *Renew Energy*. 2018 Sep;125:182–192. doi: [10.1016/j.renene.2018.02.073](https://doi.org/10.1016/j.renene.2018.02.073)
- [15] Pan H, Wu Y, Li C, et al. Efficient bi-directional OER/ORR catalysis of metal-free $\text{C}_6\text{H}_4\text{NO}_2/\text{g-C}_3\text{N}_4$: density functional theory approaches. *Appl Surf Sci*. 2020 Nov;531:147292. doi: [10.1016/j.apsusc.2020.147292](https://doi.org/10.1016/j.apsusc.2020.147292)
- [16] Darband GB, Aliofkhaezai M, Shanmugam S. Recent advances in methods and technologies for enhancing bubble detachment during electrochemical water splitting. *Renew Sust Energy Rev*. 2019 Oct;114:109300. doi: [10.1016/j.rser.2019.109300](https://doi.org/10.1016/j.rser.2019.109300)
- [17] Qian G, Mo Y, Yu C, et al. Free-standing bimetallic CoNiTe_2 nanosheets as efficient catalysts with high stability at large current density for oxygen evolution reaction. *Renew Energy*. 2020 Dec;162:2190–2196. doi: [10.1016/j.renene.2020.10.028](https://doi.org/10.1016/j.renene.2020.10.028)
- [18] Qin H, Zhen C, Jia C, et al. An oxidation-nitridation-denitridation approach to transform metal solids into foams with adjustable pore sizes for energy applications. *Sci Bull*. 2021 Aug;66(15):1525–1532. doi: [10.1016/j.scib.2021.04.031](https://doi.org/10.1016/j.scib.2021.04.031)
- [19] Son YJ, Kawashima K, Wygant BR, et al. Anodized nickel foam for oxygen evolution reaction in Fe-free and unpurified alkaline electrolytes at high current densities. *ACS Nano*. 2021 Jan;15(2):3468–3480. doi: [10.1021/acsnano.0c10788](https://doi.org/10.1021/acsnano.0c10788)
- [20] Li L, Hagiwara S, Jiang C, et al. Boron monosulfide as an electrocatalyst for the oxygen evolution reaction. *Chem Eng J*. 2023 Sep;471:144489. doi: [10.1016/j.cej.2023.144489](https://doi.org/10.1016/j.cej.2023.144489)
- [21] Kusaka H, Ishibiki R, Toyoda M, et al. Crystalline boron monosulfide nanosheets with tunable bandgaps. *J Mater Chem A*. 2021 Oct;9(43):24631–24640. doi: [10.1039/D1TA03307G](https://doi.org/10.1039/D1TA03307G)
- [22] Sugawara K, Kusaka H, Kawakami T, et al. Direct imaging of band structure for powdered rhombohedral boron monosulfide by microfocused ARPES. *Nano Lett*. 2023 Feb;23(5):1673–1679. doi: [10.1021/acs.nanolett.2c04048](https://doi.org/10.1021/acs.nanolett.2c04048)
- [23] Watanabe N, Miyazaki K, Toyoda M, et al. Rhombohedral boron monosulfide as a p-type semiconductor. *Molecules*. 2023 Feb;28(4):1896. doi: [10.3390/molecules28041896](https://doi.org/10.3390/molecules28041896)
- [24] Yamaoka S, Akaishi M, Kanda H, et al. Development of belt type high pressure apparatus for material synthesis at 8 GPa. *J High Press Inst Jpn*. 1992;30:249–258.
- [25] Marquez-Montes RA, Kawashima K, Son YJ, et al. Mass transport-enhanced electrodeposition of Ni–S–P–O films on nickel foam for electrochemical water splitting. *J Mater Chem A*. 2021 Feb;9(12):7736–7749. doi: [10.1039/D0TA12097A](https://doi.org/10.1039/D0TA12097A)
- [26] Xu Q, Gao W, Wang M, et al. Electrodeposition of $\text{NiS/Ni}_2\text{P}$ nanoparticles embedded in amorphous $\text{Ni}(\text{OH})_2$ nanosheets as an efficient and durable dual-functional electrocatalyst for overall water splitting. *Int J Hydrog Energy*. 2020 Jan;45(4):2546–2556. doi: [10.1016/j.ijhydene.2019.11.217](https://doi.org/10.1016/j.ijhydene.2019.11.217)
- [27] Zhao S, Wang Y, Dong J, et al. Ultrathin metal-organic framework nanosheets for electrocatalytic oxygen evolution. *Nat Energy*. 2016 Nov 28;1(12):16184. doi: [10.1038/nenergy.2016.184](https://doi.org/10.1038/nenergy.2016.184)
- [28] Cherednichenko KA, Sokolov PS, Kalinko A, et al. Optical phonon modes in rhombohedral boron monosulfide under high pressure. *J Appl Phys*. 2015 May;117(18):185904. doi: [10.1063/1.4921099](https://doi.org/10.1063/1.4921099)
- [29] Ni Z, Wang Y, Yu T, et al. Raman spectroscopy and imaging of graphene. *Nano Res*. 2008 Apr;1(4):273–291. doi: [10.1007/s12274-008-8036-1](https://doi.org/10.1007/s12274-008-8036-1)
- [30] Cai P, Huang J, Chen J, et al. Oxygen-containing amorphous cobalt sulfide porous nanocubes as high-activity electrocatalysts for the oxygen evolution reaction in an alkaline/neutral medium. *Angew Chem Int Ed*. 2017 Mar;56(17):4858–4861. doi: [10.1002/anie.201701280](https://doi.org/10.1002/anie.201701280)